Construction and Building Materials 515 (2026) 145689

Contents lists available at ScienceDirect

Construction and Building Materials

journal homepage: www.elsevier.com/locate/conbuildmat

Rational design of perlite-bauxite-based low-density ceramic proppants for hydraulic fracturing

Heng Zhang [a], Liehui Zhang [b], Zhaozhong Yang [b], Xiaogang Li [b], Fatereh Dorosti [c], Guoliang Chen [c], Jingyi Zhu [b], Jin Zhang [a,*], Hongcheng Yang [a], Hao Wang [d], Haibo Wang [e], Lei Ge [c,*]

[a] School of New Energy and Materials, Southwest Petroleum University, Chengdu 610500, China
[b] National Key Laboratory of Reservoir Geology and Development Engineering, Southwest Petroleum University, Chengdu, Sichuan 610500, China
[c] School of Engineering, Centre for Future Materials, University of Southern Queensland, Springfield, QLD 4300, Australia
[d] School of Engineering, Swinburne University of Technology, Hawthorn, SA 3122, Australia
[e] School of Vanadium and Titanium, Panzhihua University, Panzhihua 617000, China

ARTICLE INFO

Keywords:
Ceramic proppants
Lightweight design
Perlite-based
Bauxite
Mullite

ABSTRACT

To develop lightweight ceramic proppants and to promote the high-value utilization of two different forms of perlite, this study employed raw perlite and expanded perlite as partial substitutes for bauxite and fabricated low-density proppants via disk granulation followed by high-temperature sintering. The effects of perlite type, dosage (5–20 wt%), and sintering temperature (1400–1500 °C) on the microstructure and properties were systematically investigated. The results reveal that a moderate addition of raw perlite and expanded perlite significantly promotes mullite formation and reduces proppant density. However, excessive addition increases porosity, decreases the aspect ratio of rod-like mullite crystals, and induces the formation of ellipsoidal mullite, thereby elevating the breakage ratio. The optimized expanded perlite proppants sintered at 1450 °C exhibited the optimal overall performance, with a bulk density of 1.46 ± 0.01 g/cm^3 and an acid solubility of 5.98 ± 0.09 %. The breakage ratio of 8.21 ± 0.56 % under the industry-standard closure stress of 35 MPa, meeting the requirement of SY/T 51088–2014 (breakage ratio < 9 %). At a higher closure stress of 41.4 MPa, the proppants achieve a conductivity of 29.435 μm^2·cm. Notably, Fe^{3+} incorporation into the mullite structure enhanced structural stability, thereby improving mechanical performance. This work demonstrates a sustainable strategy for fabricating low-density ceramic proppants and highlights the potential of perlite-based materials as an environmentally friendly substitute for bauxite in hydraulic fracturing applications.

1. Introduction

Hydraulic fracturing technology has been widely employed to enhance the productivity of low-permeability reservoirs. This technique relies critically on injected proppants, which form stable, porous channels within induced fractures to maintain long-term fracture conductivity [1]. Compared with natural quartz sand, ceramic proppants offer higher mechanical strength, superior chemical stability, and more uniform particle size and sphericity, making them better suited to reservoir conditions characterized by high temperature and closure stress [2]. Conventional ceramic proppants are typically fabricated from high-grade bauxite with minor additives via disk granulation followed by high-temperature sintering. However, the high Al_2O_3 content of bauxite results in elevated sintering temperatures and increased material density. According to the Stokes law, the settling velocity of proppants increases with particle density. Therefore, dense particles tend to settle rapidly, potentially causing premature deposition and blockage within fractures, which diminishes fracture conductivity [3]. Although the use of high viscosity fracturing fluids can mitigate this issue, it substantially increases operational costs and may cause irreversible reservoir damage [4]. Moreover, the emergence of supercritical CO_2 fracturing has intensified the demand for lightweight proppants due to the inherently low viscosity of CO_2 [5]. Previous studies have demonstrated that low-density proppants can extend transport distance and enhance fracture support efficiency [6].

To develop lightweight proppants, two primary strategies have been

* Corresponding authors.
E-mail addresses: jzhang@swpu.edu.cn (J. Zhang), lei.ge@unisq.edu.au (L. Ge).

https://doi.org/10.1016/j.conbuildmat.2026.145689
Received 3 November 2025; Received in revised form 27 January 2026; Accepted 18 February 2026
Available online 19 February 2026

explored: structural modification and raw material optimization [7]. The former involves designing hollow or porous structures to reduce density, while stress concentration around voids often compromises particle strength [8]. In contrast, the latter approach partially substitutes bauxite with low-cost industrial solid wastes that possess similar chemical compositions, such as silica-rich by-products including coal gangue, fly ash, and red mud, thereby achieving density reduction while maintaining acceptable mechanical performance. For instance, Ren et al. [9] developed proppants with a bulk density of 1.352 g/cm^3 and a breakage ratio of 5.3 % at 35 MPa by replacing 30 % of bauxite with fly ash. Zhao et al. [10] synthesized proppants from bauxite, fly ash, and coal gangue with MnO_2 and MgO additives, demonstrating an apparent density of 1.03 g/cm^3 and a breakage ratio of 8.3 % at 35 MP. Similarly, Liu et al. [11] employed oil-based cuttings, red mud, and bauxite with MnO_2 to fabricate proppants with a bulk density of 1.45 g/cm^3 and a breakage ratio of 8.6 % at 52 MPa. Notably, the Fe_2O_3 in red mud facilitated the formation of closed pores, thereby contributing to weight reduction. Our previous work demonstrated that incorporating 30 wt% coal gangues into bauxite with MnO_2–TiO_2 additives produced proppants with a bulk density of 1.88 g/cm^3 and a breakage ratio of 2.71 % at 52 MPa [12].

Raw perlite, a volcanic glassy rock rich in SiO_2 and Al_2O_3, typically contains 90–97 % amorphous phases and 3–10 % crystalline phases [13]. When heated to 800–1100 °C, perlite undergoes rapid expansion due to water vaporization, yielding porous particles with volumes 5–20 times those of the original particles, forming a lightweight and porous structure. Owing to these features, perlite and its expanded form have been widely applied in insulation materials, lightweight concrete [14], ultrafiltration membranes [15], and horticulture substrates [16]. However, their applications in the ceramic field remain relatively limited. In ceramics systems, perlite is most commonly used as a pore-forming agent. Rzepa et al. [17] prepared porous ceramics with excellent thermal insulation by co-firing perlite and clay, while Tarhan et al. [13] found that perlite addition improved sintering shrinkage and mechanical strength in kaolinite systems. In ceramic proppant raw material systems, coal fly ash exhibits significant variability in chemical composition and morphological features due to differences in combustion modes, fuel composition, and operating conditions [18,19]. In addition, certain fly ashes contain appreciable amounts of SO_3, which can decompose and release gaseous species during high-temperature sintering, thereby inducing abnormal pore formation and structural defects that are detrimental to the stable development of mechanical properties [20], while red mud is enriched in heavy metal elements that pose potential environmental and health risks [21], thereby limiting their application in high-performance proppants. In contrast, perlite contains no volatile or harmful components and is rich in alkali metal oxides and SiO_2, enabling it to act simultaneously as a fluxing agent and a promoter of mullite formation, while its glassy structure and controllable expansion behavior offer new possibilities for the structural design of lightweight, high-strength ceramic proppants. However, the role of perlite (and expanded perlite) in ceramic proppant systems has not yet been systematically investigated, particularly with respect to the valence-state evolution of iron oxides during sintering and its influence on phase evolution and property regulation.

To address the knowledge gap in applying perlite as an additive in bauxite-based proppants and to elucidate the role of iron's chemical states during high-temperature sintering, this study incorporates 5–20 wt% perlite or expanded perlite into bauxite-based formulations to fabricate low-density ceramic proppants through optimized compositions and sintering regimes. The effects of perlite type, dosage, and sintering temperature on phase evolution, microstructure, bulk density, breakage ratio, and acid solubility were systematically evaluated. Furthermore, the conductivity of the obtained proppants was assessed under closure stress. This work not only expands the utilization pathway of perlite-based materials but also provides theoretical and technical insights into the rational design of lightweight ceramic proppants for hydraulic fracturing applications.

2. Experimental

2.1. Materials

Bauxite (65 wt% Al_2O_3, 200 mesh, Zhengzhou Ruiyide New Materials Co., China) and perlite/expanded perlite (325 mesh, Xinyang Yongkai Thermal Insulation Materials Co., China) were used as the primary raw materials. The chemical composition of the three raw materials was analyzed by X-ray fluorescence, and the results are summarized in Table 1. The analysis indicates that SiO_2 and Al_2O_3 are the predominant components in bauxite, perlite, and expanded perlite. Phase composition was examined using X-ray diffraction, as shown in Figure S1. Bauxite primarily consisted of corundum and mullite, with minor aluminum phosphate. In contrast, perlite and expanded perlite exhibited broad, featureless diffraction patterns, characteristic of an amorphous structure, indicating that their main phase exists in a glassy state. Morphological features of the raw materials were observed via scanning electron microscopy, as illustrated in Figure S2. Natural perlite appeared as blocky particles, whereas expanded perlite, subjected to ball milling, exhibited sheet-like morphology due to the collapse of its original hollow structure. During ball milling, sodium hexametaphosphate (analytical grade, Chengdu Kelong Chemical Reagent Co., China) was used as a dispersant to prevent agglomeration. Polyvinyl alcohol (PVA, AR, Chengdu Kelong Chemical Reagent Co., China) was employed as a binder during the granulation stage. The quartz sand and commercial proppants (40–70 mesh) used to test fracture flow capacity were sourced from Sichuan Bingyang Technology Co., Ltd.

2.2. Proppant preparation

The preparation procedure of the ceramic proppants is illustrated in Fig. 1. Initially, the raw materials were wet-milled using a planetary ball mill (QM-QX04, Zhejiang Jiechen Instrument Co., China) at a rotation speed of 300 r/min for 6 h. The mass ratio of powder, milling balls, and deionized water was 1:2:2. The resulting slurry was dried in an electric blast oven (101A-2ET, Shanghai Experimental Instrument Factory, China) at 140 °C for 24 h. The dried powder was then ground, passed through a 350-mesh sieve (≈40 μm), and its particle size distribution was measured using a laser particle size analyzer (Mastersizer-2000, Malvern Instruments Ltd.), yielding a D50 of 1.27 μm (Figure S3b). A portion of the powder was granulated in a coating machine (BY-300A, Guangzhou Daxiang Electronic Machinery Co., China) at 50 r/min. During granulation, 1.5 wt% PVA solution was added in stages with the powder until the target granule size was achieved. Granules with particle sizes corresponding to 40–70 mesh were collected, dried in an oven for 4 h, and pre-calcined at 600 °C for 30 min to remove the binder. Final sintering was carried out in a tubular furnace (STG-60–17, Henan Sante Furnace Technology Co., China) under the following schedule: heating from room temperature to 1000 °C at 5 °C/min, further heating to the target sintering temperature at 3 °C/min, followed by a 90 min dwell at the final temperature. Detailed experimental parameters are provided in Table S1. Representative samples were selected for analysis. First, the effects of different raw perlite and expanded perlite contents on the properties of the proppants were investigated at a single temperature. The influence of sintering temperature on the performance of raw perlite and expanded perlite proppants was then studied. To more effectively evaluate the effect of sintering temperature on the performance of different perlite-based proppants, the maximum additive amount that yielded a breakage ratio below 9 % was selected for each case.

For clarity, the raw materials and proppant samples were distinguished using simplified abbreviations. Expanded perlite, bauxite, and raw perlite raw materials were denoted as EP, B, and RP, respectively. The proppant samples were named according to their dominant aggregate type. Proppants prepared using expanded perlite as the aggregate

Table 1
Chemical composition of raw materials (wt%).

	Al_2O_3	SiO_2	TiO_2	Fe_2O_3	K_2O	CaO	MgO	Na_2O	Other
Bauxite	68.88	19.83	3.30	5.05	0.41	1.01	0.18	0.18	1.16
Perlite	12.08	67.19	0.06	0.82	3.34	1.20	0.96	1.27	13.08
Expanded perlite	13.97	75.37	0.10	0.64	5.56	0.94	0.26	3.02	0.14

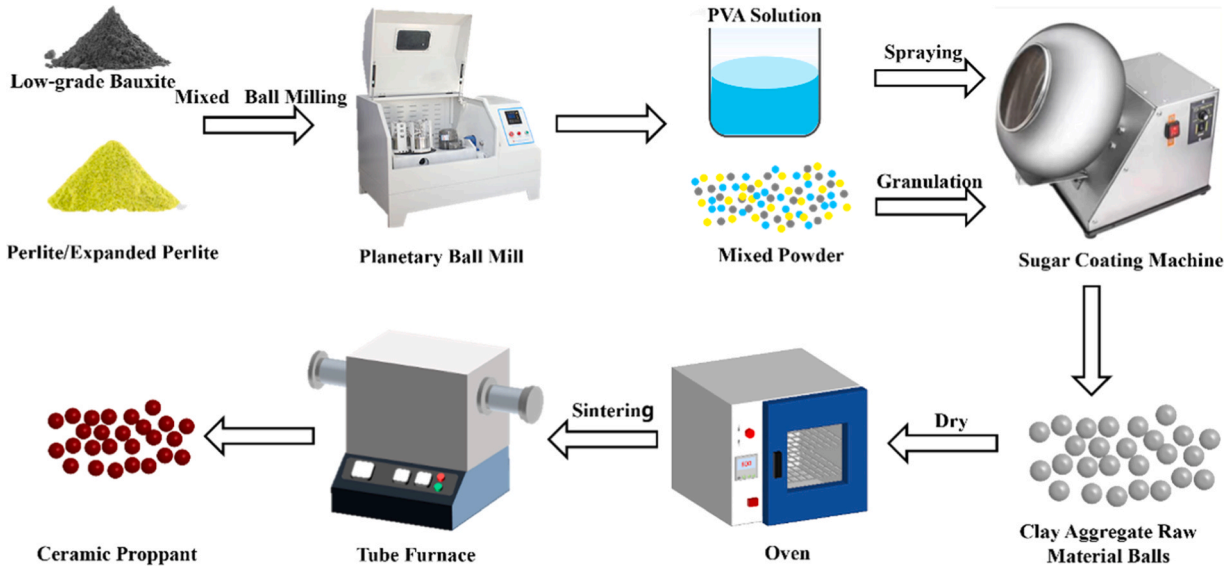

Fig. 1. Schematic illustration of the fabrication process of ceramic proppants.

were labeled EP1–EP6, those prepared proppants with raw perlite were labeled RP1–RP8, and the proppant fabricated solely from bauxite was denoted as BP. The detailed compositions are listed in Table 2.

2.3. Materials characterization

The phase composition of the proppants was analyzed by X-ray diffraction (XRD , Bruker D8 Advance) over 10–80° with a step size of 0.02°. Phase identification and semi-quantitative analysis were performed using HighScore software. The macroscopic morphology of the proppants was observed with a stereomicroscope (SZM7045, Sunny Optical Co., Ltd.). For microstructural analysis, the samples were cold-mounted, polished, and etched, then examined using a field-emission scanning electron microscope (FE-SEM, Thermo Scientific Apreo 2) coupled with an energy-dispersive X-ray spectrometer (EDS, OXFORD ULTIM Max65) to characterize the cross-sectional morphology and elemental distribution. Pore structure and grain size were quantified using ImageJ Pro Plus. Key performance metrics, including breakage ratio, bulk density, apparent density, acid solubility, and sphericity, were measured in accordance with the Chinese Petroleum and Natural Gas Industry Standard SY/T 5108–2014 for hydraulic fracturing and proppant evaluation. The breakage ratio, bulk density, apparent density, and acid solubility tests were each repeated three, five, three, and three times, respectively. The fracture conductivity of the proppants was assessed according to SY/T 6302–2019 using an NF-3 long-term conductivity tester under sequential closure stresses of 6.9, 13.8, 27.6, 41.4, 55.2, and 69 MPa, each applied for 10 min, and the corresponding fracture conductivity was recorded. The chemical states of Fe and Ti ions were determined using X-ray photoelectron spectroscopy (XPS, Nexsa, Thermo Scientific), with all spectra calibrated to the C1s peak at 284.6 eV.

Table 2
Proppant sample naming and process temperature.

Proppant Sample Abbreviations	Expanded perlite/perlite addition content (wt%)	Sintering temperature (°C)
BP	0	1450
EP1	5	1450
EP2	10	1450
EP3	15	1450
EP4	20	1450
EP5	15	1400
EP6	15	1500
RP1	5	1450
RP2	10	1450
RP3	15	1450
RP4	20	1450
RP5	5	1400
RP6	5	1500
RP7	20	1500
RP8	20	1400

3. Results and discussion

3.1. Phase analysis of ceramic proppants

Fig. 2 illustrates both the macroscopic advantages and the phase evolution mechanism of the lightweight proppants. In hydraulic fracturing operations, conventional high-density proppants exhibit limited transport distance within the fracture network and require the use of viscous thickening agents to maintain suspension, thereby increasing operational costs and potentially causing water contamination [4]. In contrast, lightweight proppants with lower bulk density exhibit superior suspension and long-distance transportability, leading to cleaner, more efficient fracturing processes (Fig. 2a). This performance improvement originates from the compositional and structural design of the proppants. As shown in the XRD patterns, all samples exhibit two primary phases: corundum (PDF#98–016–0605) and mullite (PDF#98–004–3297). In Fig. 2b, a characteristic diffraction peak of Fe-enriched mullite appears at approximately 37°, indicating that under

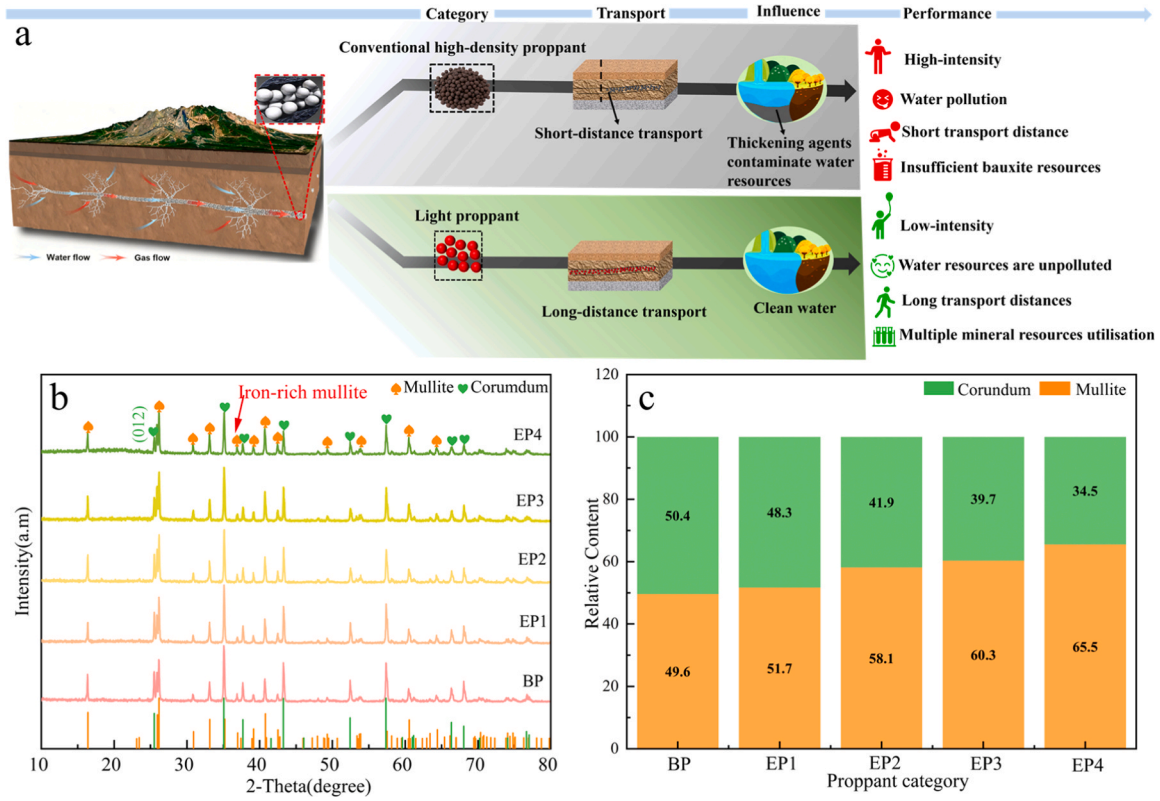

Fig. 2. Macroscopic transport advantages and the microscopic phase-evolution mechanism of lightweight proppants. (a) Schematic illustration of the transport behavior difference between conventional and lightweight proppants during hydraulic fracturing. (b) XRD patterns of ceramic proppant BP-EP4. (c) Semi-quantitative analysis of mullite and corundum phases in BP-EP4.

the present sintering conditions, Fe ions can be stably incorporated into the mullite crystal structure [22,23]. With increasing EP content, the intensity of mullite diffraction peaks gradually increases, whereas the corundum peaks, particularly the (012) crystalline surface, significantly decrease, demonstrating the strong dependence of phase assemblage on raw material composition. Semi-quantitative analysis using HighScore software (Fig. 2c) confirms that the relative mullite content increases with increasing EP fraction, while the corundum content decreases. This phase evolution trend is likely associated with the variation in the Al/Si ratio of the raw material system. The Al_2O_3/SiO_2 mass ratio of low-grade bauxite is 3.47, which decreases to 2.05 at 20 wt% addition for EP, respectively (Table 1). The increased SiO_2 content in the system promotes mullite formation, consistent with a previous report [24]. Furthermore, at identical addition levels, the phase and relative phase contents in EP- and RP-based proppants exhibit similar trends (Figure S4), indicating that despite the structural differentials between EP and RP, the comparable Al/Si ratios result in analogous phase evolution during sintering.

Fig. 3 shows the XRD patterns of proppants incorporating 15 wt% EP sintered at different temperatures. The dominant phases are identified as corundum (PDF#98–016–0605) and mullite (PDF#98–004–3298). At 1500 °C, the emergence of β-Al_2O_3 is observed, which can be ascribed to the presence of Na_2O in the raw materials. Na_2O promotes the partial transformation of α-Al_2O_3 into β-A_2O_3 during high-temperature

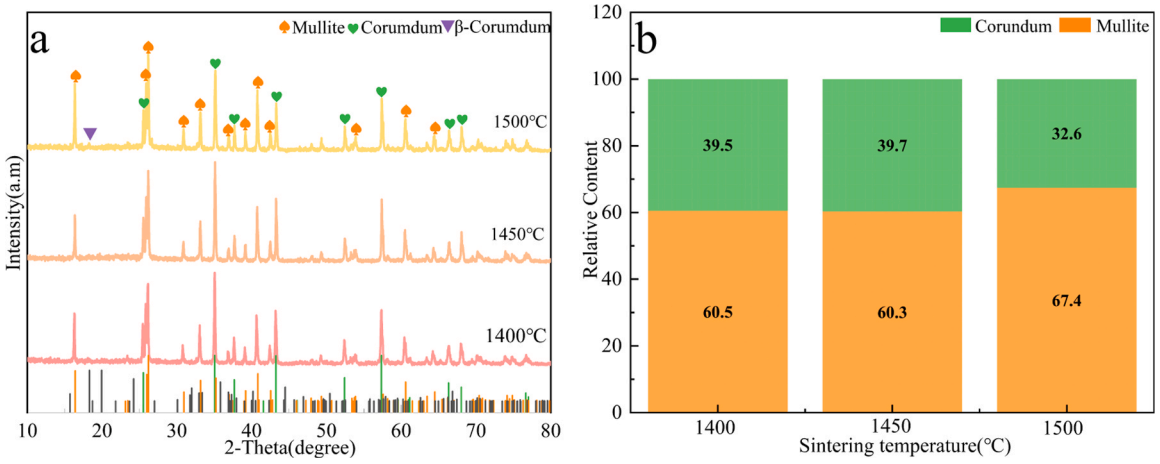

Fig. 3. XRD characterization and phase composition of adding 15 wt% EP ceramic proppant samples at different sintering temperatures. (a) XRD patterns of the ceramic proppants. (b) Semi-quantitative analysis of mullite and corundum phases in the ceramic proppants.

sintering [25]. This interpretation is further supported by EDS analysis (Figure S5), which reveals trace amounts of Na within the corundum phase. As the sintering temperature increases, the diffraction intensity of mullite peaks strengthens. Semi-quantitative phase analysis (Fig. 3b) confirms a progressive increase in mullite content, reflecting the enhanced diffusion of Al^{3+} and Si^{4+} and the accelerated reaction between Al_2O_3 and SiO_2 at elevated temperatures [26]. Nevertheless, in the 1400–1450 °C range, the growth rate of mullite formation decreases. This phenomenon is most likely related to the presence of alkali oxides such as K_2O and Na_2O, which form a viscous glassy phase at relatively low temperatures. The glassy phase encapsulates unreacted particles, hindering further migration of Al and Si ions and thereby suppressing mullite development [27]. As reported by Wang et al. [28], each 1 wt% increase in K_2O raises the liquid-phase fraction by 3–5 wt%, while Na_2O exerts an even stronger effect [29]. In line with this, EDS mapping (Figures S6, S7) demonstrates that Na and K are predominantly concentrated in the glassy phase, thereby confirming their critical role in liquid-phase generation during sintering. A comparable trend is also observed in samples containing 5 wt% RP sintered at 1400, 1450, and 1500 °C (Figure S8), further validating the above interpretation.

3.2. Morphological analysis of ceramic proppants

Fig. 4 shows the macroscopic morphology of proppants containing 20 wt% RP sintered at different temperatures (1400–1500 °C). The sphericity and roundness of the proppant particles were evaluated using the Krumbien/Sloss template method [30]. The results indicate that all samples exhibit an average sphericity greater than 0.8, meeting the technical requirement of roundness and sphericity ≥ 0.7 as specified in the Chinese petroleum and natural gas industry standard SY/T5108–2014. Visually, the proppants appear light red, with the color gradually deepening as the sintering temperature increases. This phenomenon is likely related to the high-temperature behavior of Fe_2O_3 in the raw materials, which can undergo partial reduction at elevated temperatures, thereby influencing both the color and certain properties of the final proppant [31,32].

Fig. 5 presents cross-sectional SEM images of the proppants containing different mass fractions (0–20 wt%) of EP after acid etching at 1450 °C. All samples exhibit distinct porous structures, and the porosity increases progressively with increasing EP content. This trend is likely associated with a decrease in the Al/Si ratio in the raw materials, leading to an increased proportion of amorphous phases and a reduced degree of crystallization, thereby inhibiting complete densification of the samples [33]. The sample without perlite addition shows the most compact microstructure, with the lowest porosity (4.24 %, Table S2a). In this case, the grain boundaries between mullite and corundum are indistinct, and the grains are densely packed, indicating extensive grain growth and effective densification during sintering [34]. With increasing EP content, the grain boundaries between mullite and corundum become progressively clearer, and the amount of blocky corundum grains decreases significantly, suggesting that part of the corundum participates in the reaction and transforms into mullite. This observation is consistent with the XRD semi-quantitative analysis, which shows an increase in mullite content accompanied by a decrease in corundum content. Correspondingly, when the EP content reaches 20 wt% (EP4), the internal porosity increases to 8.71 % (Table S2e), indicating that the introduction of EP at 1450 °C significantly impedes the densification process of the proppants.

Further microstructural analysis reveals that, with increasing EP addition, the morphology of mullite grains gradually evolves from short rod-like crystals with lengths of approximately 6–8 μm to finer crystals of 2–5 μm, accompanied by the appearance of ellipsoidal mullite particles. This evolution indicates that the increased SiO_2 content in the raw materials suppresses the preferential growth of rod-like mullite along the c-axis, thereby hindering the formation of a typical interlocking structure [35]. Meanwhile, the reduction in mullite grain size further promotes the formation and expansion of pores [36]. The combined effects of increased porosity and degradation of the interlocking

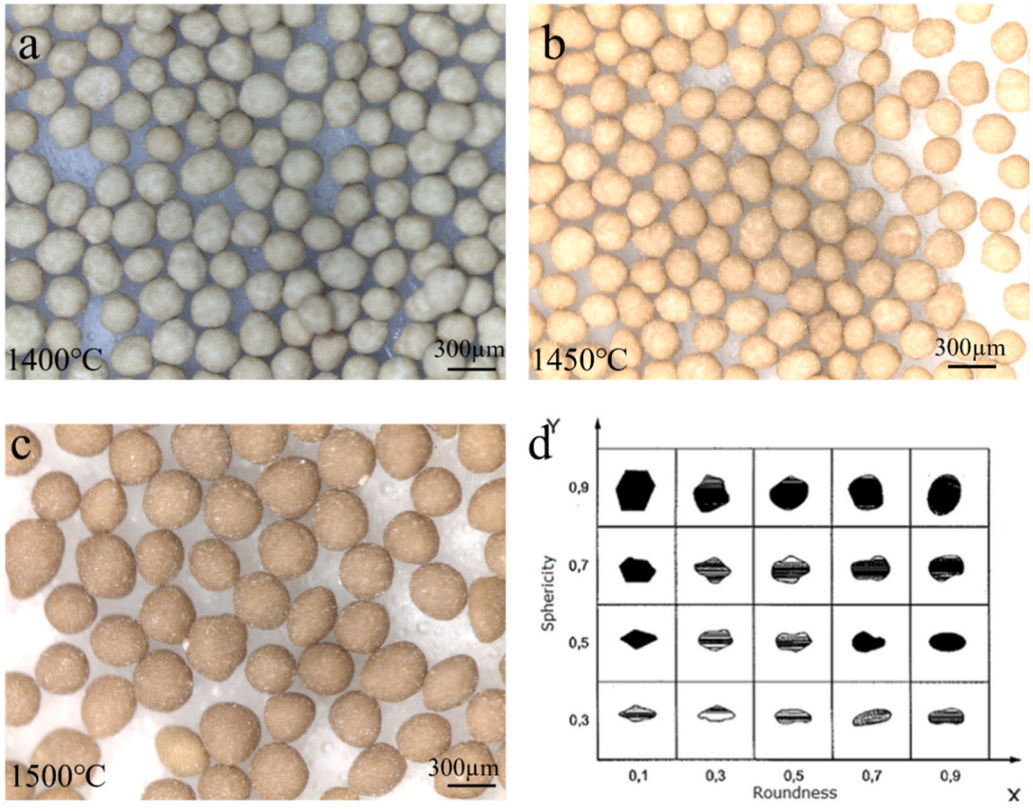

Fig. 4. Macroscopic morphology of ceramic proppants and the Krumbein/Slos template. (a) RP8, (b) RP4, (c) RP7, (d) Krumbien/Sloss template.

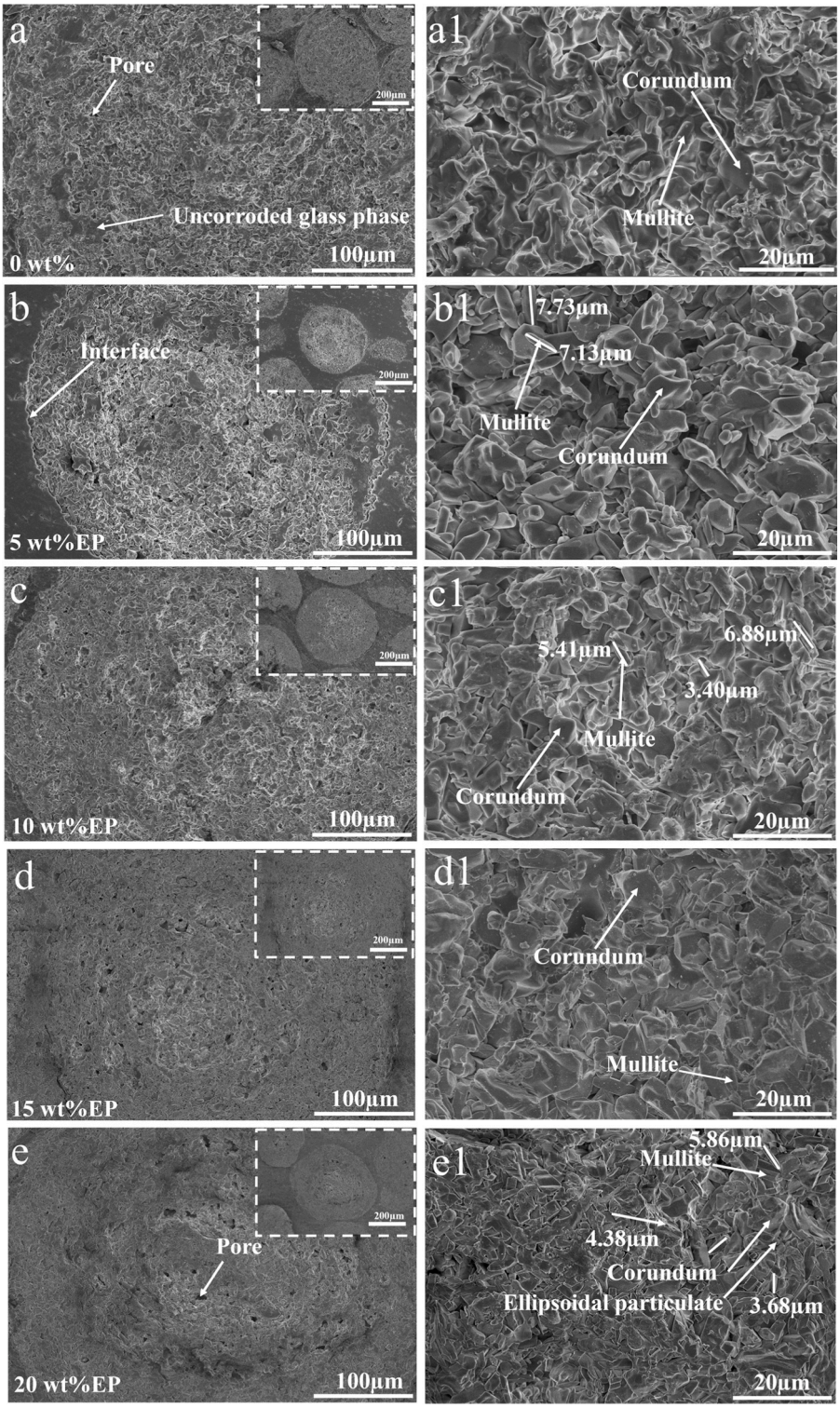

Fig. 5. Microstructures of ceramic proppants prepared at 1450 ℃ with varying mass fractions of EP. (a) BP added; (b); EP1; (c) EP2; (d) EP3; (e)EP4.

structure ultimately lead to a deterioration in the crushing resistance of the proppants. In addition, alkali metal oxides such as Na_2O and K_2O introduced by EP act as fluxing agents during sintering, facilitating the formation of a silica-rich glassy phase. Consequently, besides the commonly observed glassy and corundum phases, micron-scale mullite agglomerates can be identified in the microstructure (Fig. 5e1), which is consistent with SEM observations reported for glass–ceramics and porcelain stoneware systems [37].

By comparison, under the same mass fraction conditions, RP-based proppants exhibit a highly similar trend in microstructural evolution to that of EP-based samples (Figure S9). As the RP content increases, the degree of densification is likewise significantly reduced. Notably, when the RP content reaches 10 wt%, ellipsoidal mullite particles with markedly reduced grain size begin to appear (Figure S9b1), accompanied by a pronounced weakening of the interlocking structure. In the RP4 proppant, such ellipsoidal particles become more prevalent (Figure S9d1), corresponding to a significant increase in the breaking ratio. These results indicate that, under comparable chemical

compositions, the influence of perlite morphology on the overall microstructural evolution mechanism of the proppants is relatively limited, while their performance is predominantly governed by phase composition and crystal growth behavior regulated by the Al/Si ratio [38].

Fig. 6 presents the cross-sectional SEM images of proppants containing 15 wt% EP after acid treatment at different sintering temperatures. The porosity of the proppants first decreases and then slightly increases, while the overall densification of the structure becomes evident with increasing sintering temperature, as shown in Table S3. At 1400 °C, pores are mainly concentrated in the central region of the particles, while the outer layers exhibit higher densification (Fig. 6a). At 1450 °C, the central region densifies significantly. This evolution is likely associated with the heat-transfer mechanism during sintering: the particle surface directly absorbs radiative heat, whereas the interior is heated primarily by conduction, creating a radial temperature gradient. As a result, the outer layer densifies first, while the center initially lags behind in reaching the critical densification temperature. Further increasing the sintering temperature compensates for this temperature difference, promoting internal densification and enhancing the overall structural uniformity and compactness [39]. In addition, short rod-like mullite crystals (3–4 μm) are observed in the sample sintered at 1400 °C (Fig. 6a1). At 1500 °C, mullite grains grow further, forming numerous interwoven columnar structures with lengths of 7–13 μm (Fig. 6c1). These well-developed columnar mullite crystals exhibit strong interlocking ability, working synergistically with Al_2O_3 particles to construct a three-dimensional network, which significantly improves the material's densification and mechanical performance. Therefore, an appropriate sintering temperature not only facilitates the formation and growth of mullite crystals but also plays a crucial role in structural densification and performance enhancement [40].

Fig. 7 shows the cross-sectional SEM images of proppants containing 5 wt% RP after acid treatment at different sintering temperatures. At 1400 °C (Fig. 7a1), the microstructure is dominated by granular mullite with relatively small crystal sizes, indicating the initial stage of mullite crystallization [41]. Locally, a few rod-like mullite crystals measuring 3.25–8.70 μm in length are observed, alongside large pores with diameters ranging from 36.74 to 40.76 μm within the particle cores. The overall porosity is 14.26 % (see Figure S10a), suggesting incomplete mullite crystallization and relatively low structural densification at this temperature. When the sintering temperature is increased to 1450 °C, granular mullite largely disappears, while rod-like mullite grains grow significantly to 8–12 μm in length, exhibiting a more well-defined crystal morphology. Concurrently, the internal structure of the proppants becomes denser [42]. At 1500 °C, transition metal oxides and alkali metal oxides generate a substantial liquid phase during sintering, which accelerates densification via a viscous flux mechanism [43]. This further promotes particle densification, reduces the number of pores, and leads to a more uniform pore distribution, with overall porosity decreasing to 7.1 % (see Figure S10c).

3.3. Influence of Fe/Ti oxidation states on proppant performance

Based on the experimental results (Table S4), it was observed that ceramic proppants prepared with 20 wt% RP exhibit significant differences in breakage ratio when sintered at 1450–1500 °C. EDS analysis (Figures S11 and S12) indicates that Fe is distributed in both corundum and mullite phases, with mass fractions exceeding those of Ti, Na, and K. Correspondingly, the macroscopic color of the proppants gradually deepens to a dark red with increasing sintering temperature (Fig. 4),

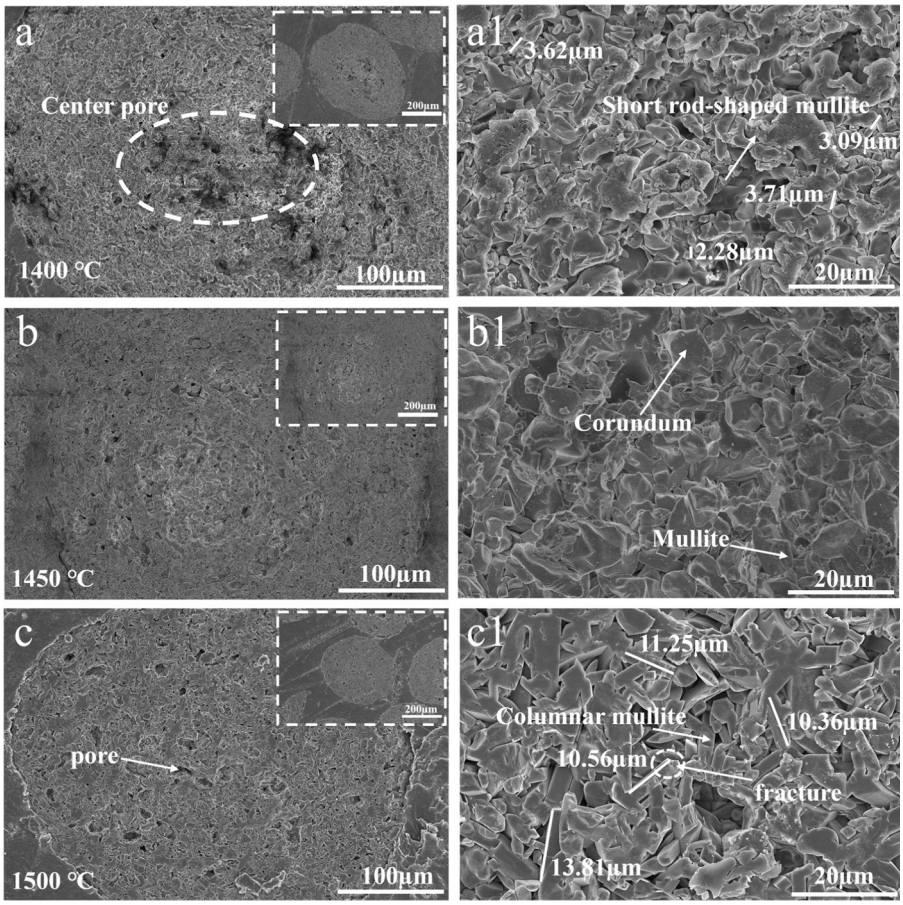

Fig. 6. SEM images of ceramic proppants prepared with 15 wt% EP at different sintering temperatures.

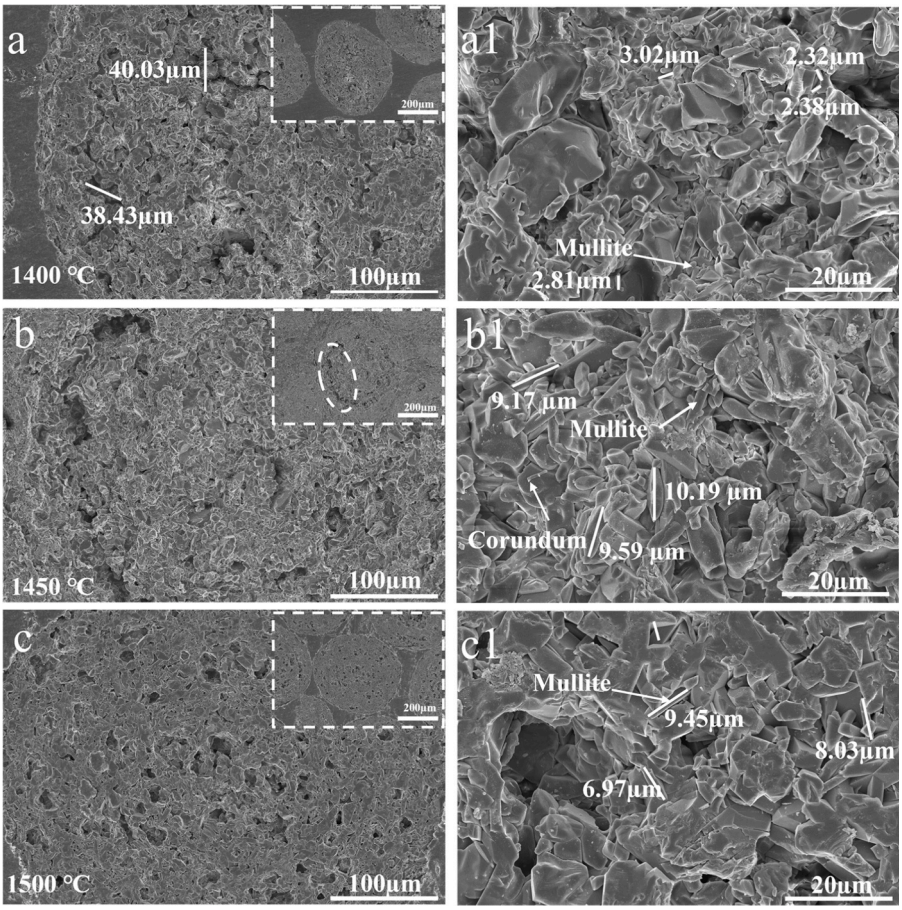

Fig. 7. SEM images of ceramic proppants prepared with 5 wt% RP at different sintering temperatures.

while the breakage ratio decreases, suggesting that Fe plays a critical role in regulating the mechanical performance of the proppants.

To further investigate the changes in the chemical valence states of Fe, Ti, and other elements before and after sintering, and their influence on proppant performance, samples prepared with 20 wt% RP were sintered at 1450 °C and 1500 °C and analyzed by X-ray photoelectron spectroscopy (XPS) for Al, Si, O, Fe, and Ti. As shown in Fig. 8a, the overall XPS survey signal intensity increases with sintering temperature, indicating that higher temperatures promote particle diffusion and pore filling, thereby enhancing the sample density and reducing porosity [44]. Deconvolution of the O 1 s peak (Fig. 8b) reveals that lattice oxygen content increases with temperature, while the concentration of oxygen vacancies decreases significantly. This is likely due to enhanced grain boundary connectivity at elevated temperatures, facilitating oxygen migration and vacancy rearrangement, and thereby reducing oxygen vacancy density [45]. Figs. 8c and 8d show that Fe exists in both Fe^{2+} and Fe^{3+} states, while Ti is predominantly present as Ti^{4+}. With increasing temperature, the relative proportion of Fe^{3+} increases markedly, likely resulting from further oxidation of Fe^{2+} at 1500 °C. This trend correlates with the decrease in oxygen vacancy concentration, confirming that high-temperature sintering promotes Fe^{2+} oxidation. Moreover, the smaller ionic radius of Fe^{3+} (65 pm) compared to Fe^{2+} (77 pm) and its closer match to Al^{3+} (54 pm) favors its substitution into the mullite structure, enhancing structural stability and proppant densification [46]. Ti^{4+} similarly substitutes for Al^{3+}in the $[AlO]_6$ octahedra of mullite, promoting crystal growth [47]. The progressive darkening of the proppant color with increasing sintering temperature (Fig. 4) further corroborates the change in the oxidation state of Fe.

The sintering process and subsequent mullitization are shown in Fig. 8e, as evidenced by the XRD, SEM, and XPS results. Owing to the relatively low melting temperature of perlite (~1200 °C) and the high content of transition metal oxides in both bauxite and perlite, the system undergoes a transformation from solid–solid sintering to liquid–solid sintering. In the range of 1200–1400 °C, the liquid phase begins to envelop the surfaces of quartz and corundum particles, facilitating the formation of mullite nuclei at the liquid–solid interface. Subsequently, at 1400 °C, elliptical mullite crystals are formed, which progressively grow with increasing sintering temperature, and transform into columnar mullite at 1500 °C.

3.4. Evaluation of derived low-density ceramic proppants

Fig. 9 illustrates the effect of EP on the performance of ceramic proppants. Panel (a) shows the influence of EP content, while panel (b) shows the effect of sintering temperature on EP3 proppants. In Fig. 9a, with increasing EP content, both bulk density and apparent density gradually decrease, whereas the breakage ratio increases. Combined with the SEM observations in Fig. 5 and the semi-quantitative phase analysis in Fig. 2, higher RP/EP content leads to increased internal porosity and promotes a higher mullite phase fraction. Since the density of mullite (3.165 g/cm^3) is lower than that of corundum (3.8–4.05 g/cm^3), and the porosity further increases, the overall density of the proppants consequently decreases [48].

Notably, a comparison between Fig. 9a (EP-based proppants) and Figure S13a (RP-based proppants) indicates that, at the same doping level, the bulk and apparent densities of EP and RP proppants are not significantly different. Despite the large difference in raw material densities (EP: 0.8–1.3 g/cm^3; RP: 2.2–2.4 g/cm^3), the sintered samples exhibit highly consistent phase composition and microstructure, as confirmed by XRD and SEM. These results suggest that the density of

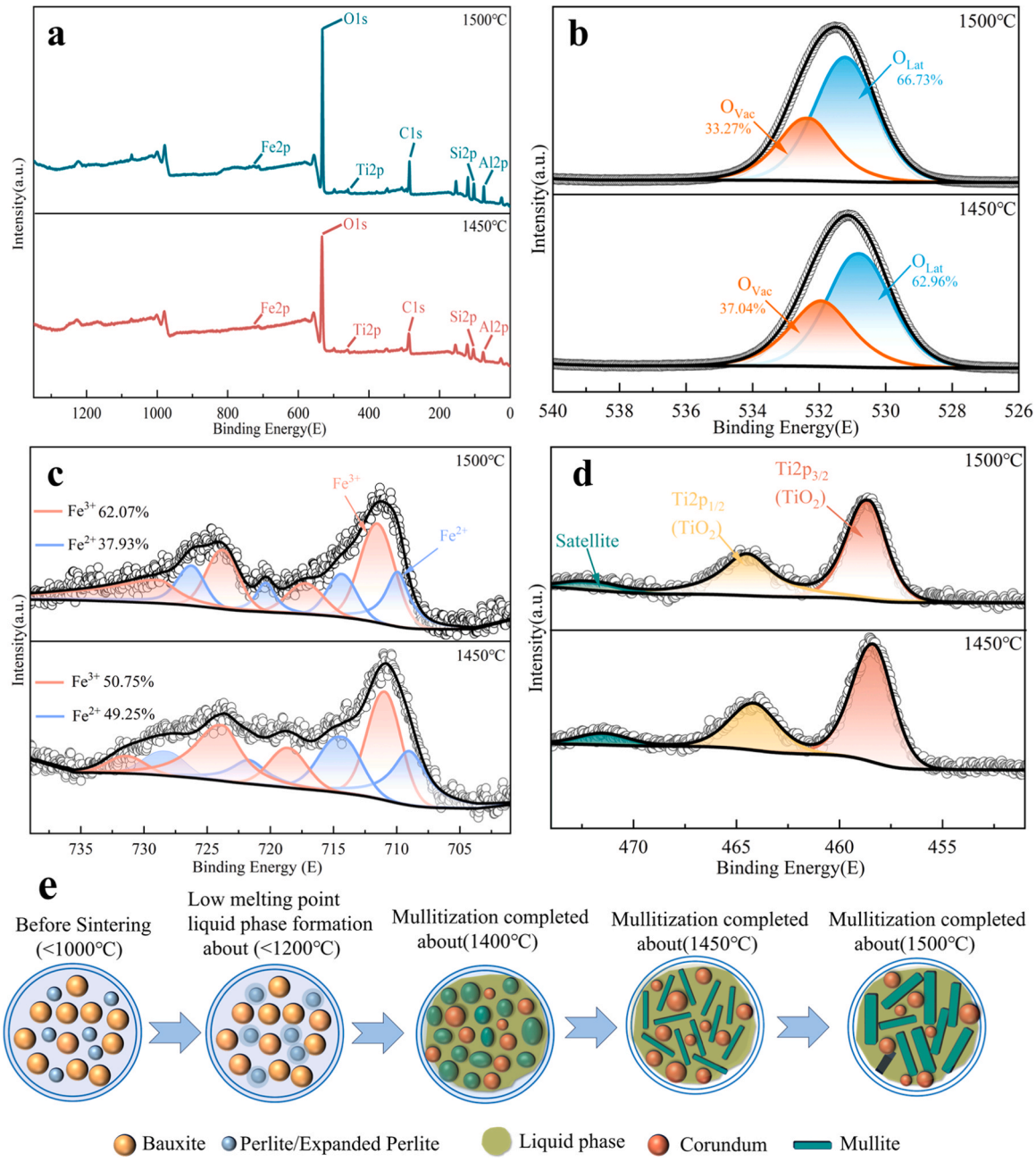

Fig. 8. X-ray photoelectron spectra (XPS) of ceramic proppants containing 20 wt% RP sintered at different temperatures (1450 °C and 1500 °C) and mullitization process: (a) survey spectra of Al, Si, O, Fe, and Ti; (b) O 1 s; (c) Fe 2p; (d) Ti 2p; (e) Sintering process model and mullitization process of the sample。.

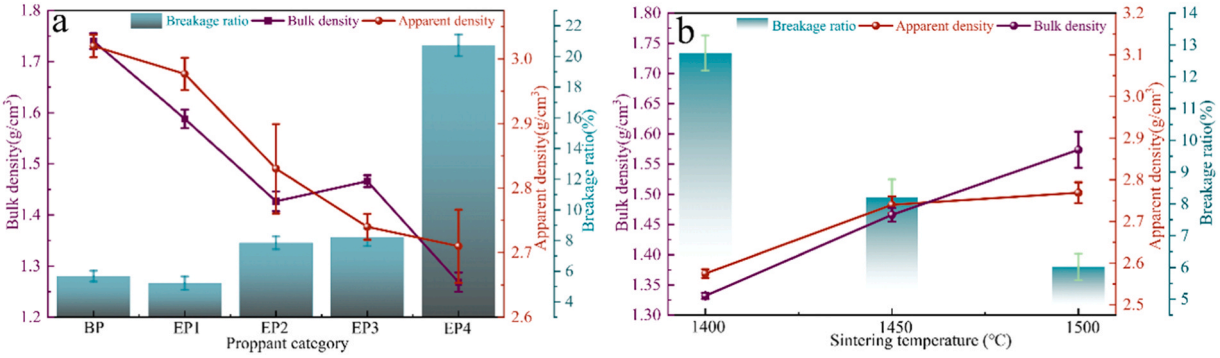

Fig. 9. Effect of EP on the performance of ceramic proppants. (a) For EP of varying concentrations; (b) For adding EP at 15 wt%.

sintered proppants is primarily governed by phase composition and structural densification rather than the intrinsic density of the raw materials. Previous studies have shown that increasing mullite content in mullite–corundum composites typically reduces overall mechanical performance [49,50]. Furthermore, with increasing RP/EP content, the porosity further increases, while acicular mullite becomes shorter and gradually transforms into elliptical grains (Figs. 5 and S9). These microstructural changes increase the presence of pores, weaken the interlocking network between grains, and provide more initiation and propagation paths for cracks, collectively reducing the breakage ratio of the proppants [36,51]. Comprehensive performance testing shows that proppants prepared with 15 wt% EP at 1450 °C exhibit a balanced combination of properties in this system: a bulk density of 1.46 ± 0.01 g/cm^3, an apparent density of 2.74 ± 0.02 g/cm^3, and a breakage ratio of 8.21 ± 0.56 % under 35 MPa closure stress.

Additionally, the influence of temperature on the performance of ceramic proppants is described. As shown in Fig. 9b and Figure S13b, increasing the sintering temperature leads to a gradual increase in both bulk and apparent densities, while the breakage ratio continuously decreases. At 1500 °C, the proppants achieve peak densities and minimum breakage ratio, indicating optimal mechanical performance. SEM analysis indicates that at 1400 °C, significant porosity remains inside the proppant, resulting in lower bulk and apparent densities. As the temperature increases, the microstructure becomes progressively denser, contributing to a marked density increase. This densification is primarily attributed to accelerated reaction kinetics at higher temperatures, promoting pore elimination and volumetric shrinkage [52]. Furthermore, at 1400 °C, mullite mainly exists as granular particles (Figs. 6 and 7). When the sintering temperature rises to 1500 °C, mullite preferentially grows along the C-axis, gradually forming columnar structures that interlock with the corundum phase to construct a three-dimensional cross-linked network. This network significantly enhances the compressive strength of the proppants, thereby further reducing the breakage ratio [53].

3.5. Service performance of ceramic proppants

Acid solubility is a critical measure of chemical stability for proppants in acidic environments; lower values generally indicate superior corrosion resistance and longer service life [54]. Fig. 10 presents the acid solubility trends of two types of perlite-bauxite-based proppants. Fig. 10a shows the acid solubility of proppants containing varying mass fractions (0–20 wt%) of EP or RP sintered at 1450 °C. For the EP series, acid solubility first decreases and then increases with EP content. The minimum solubility of 4.99 ± 0.16 % is observed at 10 wt% EP, which can be attributed to the formation of mullite and the improved microstructure and phase distribution, enhancing overall acid resistance [55]. When the EP content increases to 20 wt%, the acid solubility rises to 6.3 ± 0.17 %, likely due to enhanced fluxing effects of transition metal oxides and increased glassy phase content, which reduces corrosion resistance [56]. In contrast, acid solubility in the RP series rises to a maximum at 10 wt% perlite before decreasing at higher contents. As per SEM (Figure S9, RP1–RP4), higher RP contents reduce rod-like mullite and increase oval-shaped mullite, concurrently tightening intergranular spacing. The denser microstructure thereby restricts acid penetration and reduces solubility. Nevertheless, the largest pores observed in the 10 wt% RP sample after acid exposure suggest that structural defects may contribute to the temporary increase in acid solubility [57]. Fig. 10b shows the acid solubility of proppants containing 15 wt% EP and 5 wt% RP at different sintering temperatures. As the temperature increases from 1400 to 1500 °C, the acid solubility of both samples decreases significantly, indicating that higher sintering temperatures enhance acid resistance. This improvement stems from high-temperature mullite formation, via reaction of soluble silicate glass phases with Al_2O_3, along with densification of particles, which reduces pathways for acid penetration [58]. Among the samples, the one containing 5 wt% RP sintered at 1500 °C exhibits the lowest acid solubility of 3.76 ± 0.31 %.

Flow conductivity, as a key evaluation metric in hydraulic fracturing, reflects the efficiency of fluid transport within fractures and directly influences reservoir productivity [59]. Among the various factors affecting flow performance, the breakage resistance of proppants is particularly critical [60]. Based on experimental data (Table S4), three laboratory-prepared proppants-BP (breakage ratio 5.66 %), EP3 (breakage ratio 8.21 %), and RP7 (breakage ratio 3.46 %) were selected and compared with two commercial proppants: a quartz sand proppant with a bulk density of 1.58 g/cm^3 and a 35 MPa breakage ratio of 12.63 %, and a ceramic proppant with a bulk density of 1.57 g/cm^3 and a 35 MPa breakage ratio of 2.16 %. Fig. 11 compares the performance of the laboratory-made proppants with that of the commercial fracturing proppants. As shown in Fig. 11a, the fracture conductivity of all five proppants decreases with increasing closure stress, resulting from particle compaction, breakage ratio, and pore structure contraction. Notably, the commercial ceramic proppant exhibits a breakage ratio comparable to the laboratory-prepared RP7 at 35 MPa, and correspondingly shows similar fracture conductivity. In contrast, quartz sand undergoes severe crushing under high closure stress, producing fines that can block pore channels, thereby significantly reducing conductivity [61]. At a closure stress of 69 MPa, the quartz sand as well as EP3 and BP proppants display varying degrees of aggregation; however, some loose, uncrushed particles remain (Figure S14). This

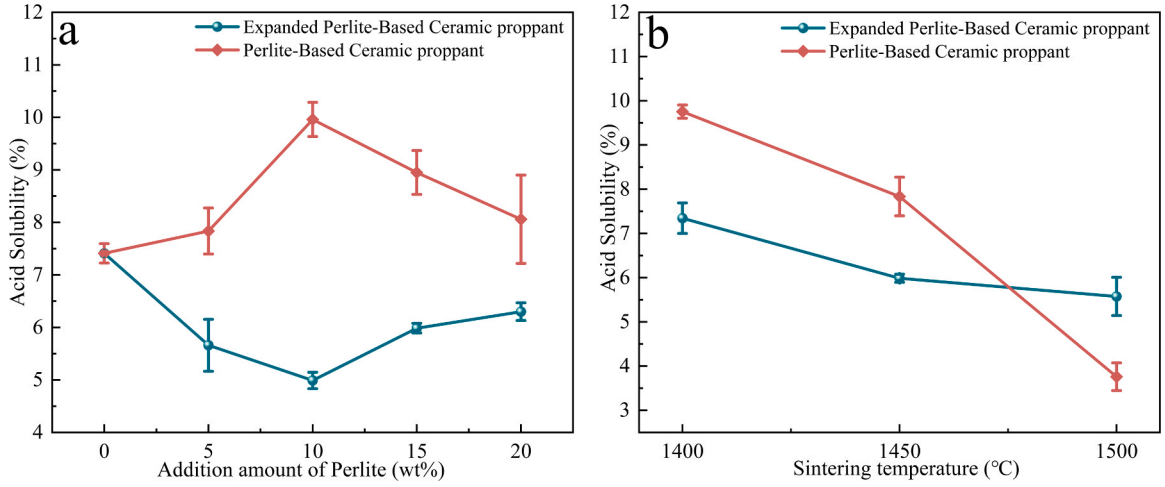

Fig. 10. (a) Acid solubility of ceramic proppants prepared at 1450 ℃ with varying mass fractions of /perlite. (b) Acid solubility curves of ceramic proppants containing 15 wt% EP and 5 wt% RP at different sintering temperatures.

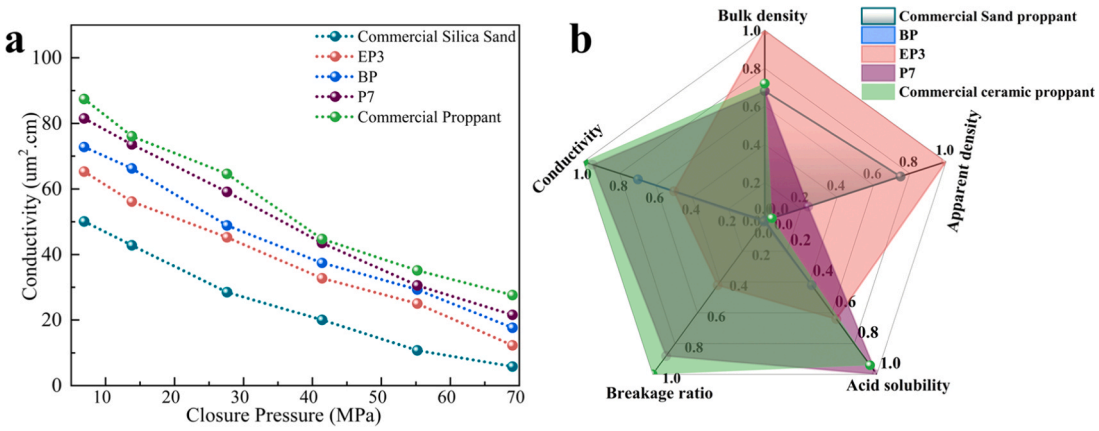

Fig. 11. Performance comparison between the bauxite/perlite-based proppant in this study and the commercial quartz sand and ceramic proppants: (a) conductivity and closure pressure relationship; (b) overall performance.

aggregated-loose structure further indicates that particle compaction and crushing increasingly impair effective flow paths under higher stress, while residual loose particles allow partial conductivity to be maintained, though at a reduced overall level [62], the underlying mechanism is illustrated in Figure S15. Fig. 11b compares the overall physical performance of the five proppants. Density, breakage ratio, and acid solubility are treated as negative indicators, whereas fracture conductivity is a positive indicator. All parameters were normalized to the 0–1 range using min–max scaling, with higher values representing superior performance [63]. The results indicate that EP3 combines low density with good mechanical strength and exhibits significantly higher fracture conductivity than quartz sand, demonstrating the best overall performance among the tested proppants.

4. Conclusion

In this study, lightweight ceramic proppants were successfully prepared by partially replacing bauxite with raw perlite (RP) and expanded perlite (EP) using disc granulation and high-temperature sintering. The incorporation of perlite effectively regulated the phase composition and microstructure, promoting mullite formation. At elevated temperatures, Fe^{3+} ions were incorporated into the mullite lattice to form Fe-enriched mullite, thereby enhancing structural stability. The proppant density was governed by the combined effects of phase composition and porosity.

(1) Effect of perlite content: With increasing perlite addition, mullite grains gradually evolved from rod-like to ellipsoidal morphologies, accompanied by increased porosity and reduced densification. At 1450 °C, when the contents of EP and RP were limited to $\leq$ 15 wt% and $\leq$ 5 wt%, respectively, ordered mullite growth was maintained, resulting in stable mechanical performance.

(2) Effect of sintering temperature: Increasing the sintering temperature to 1500 °C favored the formation of well-developed rod-like mullite and a dense interlocking structure, leading to simultaneous improvements in mechanical strength and acid resistance. XPS results indicated that the transformation of Fe^{2+} to Fe^{3+} and the reduction of oxygen vacancies at high temperatures are key factors contributing to microstructural stability and performance enhancement.

(3) Optimal composition and performance: Under optimal conditions of 15 wt% EP addition and sintering at 1450 °C, the proppant (EP3) exhibited excellent comprehensive performance, with a bulk density of 1.46 ± 0.01 g/cm^3, a breakage ratio of 8.21 ± 0.56 %, and an acid solubility of 5.98 ± 0.09 %. A fracture conductivity of 29.435 μm^2·cm was achieved at a closure stress of 41.4 MPa. This formulation achieves a balanced combination of low density, high crushing resistance, and good acid resistance, demonstrating strong potential for applications in low- to medium-closure-stress reservoirs. Overall, this study provides a clear processing window and experimental basis for the design of high-performance lightweight proppants.

CRediT authorship contribution statement

Jingyi Zhu: Writing – original draft, Validation, Formal analysis. **Jin Zhang:** Writing – review & editing, Writing – original draft, Validation, Supervision, Resources, Project administration, Methodology, Investigation, Formal analysis, Conceptualization. **Guoliang Chen:** Writing – review & editing, Writing – original draft, Data curation. **Haibo Wang:** Writing – review & editing, Data curation. **Heng Zhang:** Writing – review & editing, Writing – original draft, Visualization, Methodology, Investigation, Formal analysis, Data curation. **Lei Ge:** Writing – review & editing, Writing – original draft, Supervision, Resources, Project administration, Methodology, Funding acquisition, Formal analysis, Conceptualization. **Hongcheng Yang:** Writing – original draft, Methodology, Formal analysis. **Hao Wang:** Writing – review & editing, Project administration, Funding acquisition. **Xiaogang Li:** Writing – review & editing, Supervision, Resources, Project administration, Methodology, Investigation. **Fatereh Dorosti:** Writing – review & editing, Formal analysis, Data curation. **Liehui Zhang:** Writing – original draft, Investigation, Formal analysis, Data curation. **Zhaozhong Yang:** Writing – original draft, Supervision, Resources, Project administration.

Declaration of Competing Interest

The authors declare that they have no known competing financial interests or personal relationships that could have appeared to influence the work reported in this paper.

Acknowledgments

The authors acknowledge the financial support provided by The Key Program of the National Natural Science Foundation of China (Grant No. 52234003), the Australia Research Council Linkage project (LP200100420), and the Sichuan Vanadium and Titanium Materials Engineering Technology Research Center (25FTCLZX0004).

Appendix A. Supporting information

Supplementary data associated with this article can be found in the online version at doi:10.1016/j.conbuildmat.2026.145689.

Data availability

Data will be made available on request.

References

[1] M.R. Krishnan, W. Li, B. Alharbi, E. Alsharaeh, Recent developments on in-situ generated proppants for hydraulic fracturing operations: a critical review, Geoenergy Sci. Eng. 242 (2024) 213227, https://doi.org/10.1016/j.geoen.2024.213227.

[2] F. Liang, M. Sayed, G.A. Al-Muntasheri, F.F. Chang, L. Li, A comprehensive review on proppant technologies, Petrol 2 (2016) 26–39, https://doi.org/10.1016/j.petlm.2015.11.001.

[3] G. Zhang, M. Li, K. Geng, R. Han, M. Xie, K. Liao, New integrated model of the settling velocity of proppants falling in viscoelastic slick-water fracturing fluids, J. Nat. Gas. Sci. Eng. 33 (2016) 518–526, https://doi.org/10.1016/j.jngse.2016.05.053.

[4] J. Zhao, Y. Peng, Y. Li, W. Lei, Y. Zhang, Q. Mi, 2013, Abnormal sand Plug Phenomenon at A High Injection Rate and Relevant Solutions. 33566010.3787/j.issn.1000-0976.2013.04.009.

[5] Y. Zheng, H. Wang, H. Huang, J. Ni, B. Wang, B. Yang, W. Zhang, CFD-DEM simulation of proppant transport under variable injection strategies in rough fracture network with supercritical CO_2, Powder Technol. 457 (2025) 120856, https://doi.org/10.1016/j.powtec.2025.120856.

[6] B. Liu, A. Suzuki, T. Ito, Numerical analysis of different fracturing mechanisms between supercritical CO_2 and water-based fracturing fluids, Int. J. Rock. Mech. Min. Sci. 132 (2020) 104385, https://doi.org/10.1016/j.ijrmms.2020.104385.

[7] Z. Liao, X. Li, L. Ge, Z. Yang, J. Zhu, Q. Xue, H. Wang, Lightweight proppants in unconventional oil and natural gas development: a review, Sustain. Mater. Technol. 33 (2022) e00484, https://doi.org/10.1016/j.susmat.2022.e00484.

[8] Z. Liao, H. Rabiee, L. Ge, X. Li, Z. Yang, Q. Xue, C. Shen, H. Wang, Revealling pore microstructure impacts on the compressive strength of porous proppant based on finite and discrete element method, J. Mater. Sci. Technol. 211 (2025) 72–81, https://doi.org/10.1016/j.jmst.2024.05.054.

[9] Q. Ren, Y. Ren, H. Li, X. Wu, W. Bai, J. Zheng, O. Hai, Preparation and characterization of high silicon ceramic proppants using low grade bauxite and fly ash, Mater. Chem. Phys. 230 (2019) 355–361, https://doi.org/10.1016/j.matchemphys.2019.04.009.

[10] X. Zhao, W. Li, X. Zhang, Y. Xue, J. Mu, D. Xu, W. Li, Y. Wang, S. Qin, Z. hang, Low-temperature preparation of lightweight ceramic proppants using high-proportioned coal-based solid wastes, Ceram. Int. 50 (2024) 18117–18124, https://doi.org/10.1016/j.ceramint.2024.02.295.

[11] W. Liu, X. Xiong, Y. Zhao, C. Liu, Y. Hou, X. Pu, Preparing high-strength and low-density proppants with oil-based drilling cuttings pyrolysis residues and red mud: process optimization and sintering mechanism, Fuel 331 (2023) 125777, https://doi.org/10.1016/j.fuel.2022.125777.

[12] H. Zhang, T. Yuan, L. Zhang, Z. Yang, X. Li, F. Dorosti, J. Zhu, J. Zhang, H. Yang, H. Wang, L. Ge, MnO_2-TiO_2 composite additives driven low-cost fabrication of coal gangue/bauxite ceramic proppants, Ceram. Int. (2025), https://doi.org/10.1016/j.ceramint.2025.06.353.

[13] B. Tarhan, M. Tarhan, Utilization of perlite as an alternative raw material in the production of ceramic sanitaryware, J. Therm. Anal. Calorim. 147 (2022) 3509–3518, https://doi.org/10.1007/s10973-021-10784-5.

[14] R. Szabó, F. Dolgos, Á. Debreczeni, G. Mucsi, Scale-up experiments of expanded perlite-geopolymer composite block with special regard to the effect of water, Constr. Build. Mater. 464 (2025) 140166, https://doi.org/10.1016/j.conbuildmat.2025.140166.

[15] N.P. Fadeeva, M.V. Pavlov, I.A. Kharchenko, M.M. Simunin, K.A. Shabanova, V. F. Pavlov, I.I. Ryzhkov, High strength ceramic substrates based on perlite and foam silicates for filtration membranes, Membr. Membr. Technol. 4 (2022) 170–176, https://doi.org/10.1134/S2517751622030040.

[16] Z. Qiu, Q. Wang, J. Zhang, W. Zhou, X. Chen, X. Zhu, Comprehensive evaluation of the effects of different composite substrates on the growth of tree peony, Plant Growth Regul. 105 (2025) 861–874, https://doi.org/10.1007/s10725-025-01310-w.

[17] K. Rzepa, W. Wons, M. Reben, Building ceramics with improved thermal insulation parameters, E3S Web Conf. 10 (2016) 00082, https://doi.org/10.1051/e3sconf/20161000082.

[18] E. Strzalkowska, Morphology and chemical composition of mineral matter present in fly ashes of bituminous coal and lignite, Int. J. Environ. Sci. Technol. 18 (2020), https://doi.org/10.1007/s13762-020-03016-0.

[19] J.C. Hower, J.G. Groppo, S.D. Hopps, T.D. Morgan, H. Hsu-Kim, R.K. Taggart, Coal feed-dependent variation in fly ash chemistry in a single pulverized-combustion unit, Minerals 12 (2022) 1071, https://doi.org/10.3390/min12091071.

[20] H. Wang, L. Cheng, J. Pu, J. Zhao, Melting characteristics of coal ash and properties of fly ash to understand the slag formation in the shell gasifier, ACS Omega 6 (2021) 16066–16075, https://doi.org/10.1021/acsomega.1c01949.

[21] J. Pei, X. Pan, Y. Qi, H. Yu, G. Tu, Preparation of ultra-lightweight ceramsite from red mud and immobilization of hazardous elements, J. Environ. Chem. Eng. 10 (2022) 108157, https://doi.org/10.1016/j.jece.2022.108157.

[22] H. Ye, Y. Li, J. Sun, Study on formation mechanism and morphology evolution of Iron-exsolution mullite, Mater. Lett. 246 (2019) 9–12, https://doi.org/10.1016/j.matlet.2019.03.019.

[23] H. Ye, Y. Li, J. Sun, Y. Sun, X. Wu, M. Yan, Novel iron-rich mullite solid solution synthesis using fused-silica and α-Al_2O_3 powders, Ceram. Int. 45 (2019) 4680–4684, https://doi.org/10.1016/j.ceramint.2018.11.159.

[24] Y. Yang, H. Li, Z. Lei, H. Liu, M. Zeng, T. Yang, K. Chen, Y. Duan, Y. Duan, Preparation and characterization of high-performance ceramic proppant from recycling utilization of oil-based drilling cuttings pyrolysis residues, Sci. Rep. 14 (2024) 2345, https://doi.org/10.1038/s41598-024-52334-7.

[25] L. Yang, Y. Zeng, C. Guo, Y. Lliu, B. Li, T. Deng, W. Chen, Y. Du, Experimental investigation and thermodynamic assessment of the Na_2O–Al_2O_3–CaO system, Ceram. Int. 50 (2024) 13422–13438, https://doi.org/10.1016/j.ceramint.2024.01.255.

[26] H.J. Kleebe, F. Siegelin, T. Straubinger, G. Ziegler, Conversion of Al_2O_3–SiO_2 powder mixtures to 3:2 mullite following the stable or metastable phase diagram, J. Eur. Ceram. Soc. 21 (2001) 2521–2533, https://doi.org/10.1016/S0955-2219(01)00275-8.

[27] J.M.A. Šaponjić1, Ž. Radovanović2, M. Pošarac-Marković1, M. Gordić, Properties of durable mullite bodies manufactured from waste clay-diatomite, MMD 2 (2024), https://doi.org/10.56801/MMD32.

[28] Y.X. Wang, J.Z. Zhang, J.Y. Gao, Z.P. Yang, Modification of liquid phase and microstructure of sintered mullite by different additives, Int. J. Appl. Ceram. Technol. 22 (2025), https://doi.org/10.1111/ijac.14860.

[29] R.G. Frizzo, A. Zaccaron, V. de Souza Nandi, A.M. Bernardin, Pyroplasticity on porcelain tiles of the albite-potassium feldspar-kaolin system: a mixture design analysis, J. Build. Eng. 31 (2020) 101432, https://doi.org/10.1016/j.jobe.2020.101432.

[30] W.C. Krumbein, Measurement and geological significance of shape and roundness of sedimentary particles, J. Sediment. Res. 11 (1941) 64–72, https://doi.org/10.1306/d42690f3-2b26-11d7-8648000102c1865d.

[31] T. Hanzlicek, D. Niznansky, J. Dedecek, M. Steinerova, P. Straka, J. Triskova, Discoloration of Fired Kaolinitic Clays (Study of Fe^{3+} Coordination by Mössbauer and UV-ViS-NIR Spectroscopy), J. Am. Ceram. Soc. 90 (2007) 2843–2848, https://doi.org/10.1111/j.1551-2916.2007.01734.x.

[32] L. Yu, Y. Zhang, Z. Zhang, J. Yang, Conversion of recycled sludge waste into high value-added ceramics as engineering construction materials: fabrication, characterization and performance evaluation, Chem. Eng. J. 475 (2023) 146509, https://doi.org/10.1016/j.cej.2023.146509.

[33] M. Seiz, H. Hierl, B. Nestler, W. Rheinheimer, Revealing process and material parameter effects on densification via phase-field studies, Sci. Rep. 14 (2024) 5350, https://doi.org/10.1038/s41598-024-51915-w.

[34] H. Schneider, J. Schreuer, B. Hildmann, Structure and properties of mullite - a review, J. Eur. Ceram. Soc. 28 (2008) 329–344, https://doi.org/10.1016/j.jeurceramsoc.2007.03.017.

[35] P. Zhao, S. Ma, X. Wang, W. Wu, Y. Ou, Properties and mechanism of mullite whisker toughened ceramics, Ceram. Int. 49 (2023) 10238–10248, https://doi.org/10.1016/j.ceramint.2022.11.202.

[36] C.H.H. Hsiung, A.J. Pyzik, F. De Carlo, X. Xiao, S.R. Stock, K.T. Faber, Microstructure and mechanical properties of acicular mullite, J. Eur. Ceram. Soc. 33 (2013) 503–513, https://doi.org/10.1016/j.jeurceramsoc.2012.09.017.

[37] P.J. Sánchez-Soto, E. Garzón, L. Pérez-Villarejo, G.N. Angelopoulos, D. Eliche-Quesada, Mining wastes of an albite deposit as raw materials for vitrified mullite ceramics, Minerals 11 (2021) 232, https://doi.org/10.3390/min11030232.

[38] N.C. Chen, W. Wang, A.P. Deng, H.M. Ao, Q.H. Li, Effects of Si/Al molar ratio on morphology of mullite nanocomposite synthesized from Kaolin, Mater. Sci. Forum 682 (2011) 55–59, https://doi.org/10.4028/www.scientific.net/MSF.682.55.

[39] D. Li, Z.J. Shen, Rapid sintering of ceramics with gradient porous structure by asymmetric thermal radiation, J. Am. Ceram. Soc. 98 (2015) 3631–3634, https://doi.org/10.1111/jace.13926.

[40] H. Liu, R.-Z. Zhang, J.-M. Wu, W.-K. Li, S.-X. Zhou, J. Zhang, W. Zheng, C.-Z. Yan, S.-F. Wen, C.-S. Ye, Y.-S. Shi, C.-Y. Chen, Z.-M. Ren, Effect of $Al(OH)_3$ on the properties of silica-based ceramic cores prepared by laser powder bed fusion combined with vacuum infiltration, Addit. Manuf. 95 (2024) 104527, https://doi.org/10.1016/j.addma.2024.104527.

[41].] A. Kalemtaş, N. Özey, M.T. Aytekin Aydin, Processing of layered porous mullite ceramics, J. Aust. Ceram. Soc. 54 (2018) 545–555, https://doi.org/10.1007/s41779-018-0183-6.

[42] X. Wu, Z. Huo, Q. Ren, et, H. Li, F. Lin, T. Wei, Preparation and characterization of ceramic proppants with low density and high strength using fly ash, J. Alloy. Compd. 702 (2017) 442–448, https://doi.org/10.1016/j.jallcom.2017.01.262.

[43] H.P.A. Alves, R.A. Junior, L.F.A. Campos, R.P.S. Dutra, J.P.F. Grilo, F.J.A. Loureiro, D.A. Macedo, Structural study of mullite based ceramics derived from a mica-rich kaolin waste, Ceram. Int. 43 (2017) 3919–3922, https://doi.org/10.1016/j.ceramint.2016.12.035.

[44] A. Hajian, A. Artemenko, A. Kromka, S. Schwarz, M. Schneider, K. Dragounová, M. Adaikkan, C. Zellner, U. Schmid, Impact of sintering temperature on phase composition, microstructure, and porosification behavior of LTCC substrates, J. Eur. Ceram. Soc. 42 (2022) 5789–5800, https://doi.org/10.1016/j.jeurceramsoc.2022.05.049.

[45] C. Liu, R. Mao, Q. Wu, et, J. Li, D. Zheng, Z. Fei, C. Pang, Modification of BCZT piezoelectric ceramics by modulating oxygen vacancies in different sintering atmospheres, AIP Adv. 13 (2023), https://doi.org/10.1063/5.0155475.

[46] H. Ye, Y. Li, J. Sun, Study on formation mechanism and morphology evolution of Iron-exsolution mullite, Mater. Lett. 246 (2019) 9–12, https://doi.org/10.1016/j.matlet.2019.03.019.

[47] M. Yan, Y. Li, Y. Sun, L. Li, S. Tong, J. Sun, Controllable preparation and synthetic mechanism of mullite from the bauxite with Fe-rich oxide content, Mater. Chem. Phys. 202 (2017) 245–250, https://doi.org/10.1016/j.matchemphys.2017.09.017.

[48] R. Roy, D. Das, P.K. Rout, A review of advanced mullite ceramics, Eng. Sci. 18 (2022) 20–30, https://doi.org/10.30919/es8d582.
[49] Ting-shou Li, Geng-chen Sun, Study on high temperature mechanical properties of mullite-corundum sintered materials, Refractories 23 (02) (1989) 9–12.
[50] A.V. Maldhure, H.S. Tripathi, A. Ghosh, Mechanical properties of Mullite-Corundum composites prepared from bauxite, Int. J. Appl. Ceram. Technol. 12 (2015) 860–866, https://doi.org/10.1111/ijac.12291.
[51] R. Zhang, C. Ye, X. Hou, S. Li, B. Wang, Microstructure and properties of lightweight fibrous porous mullite ceramics prepared by vacuum squeeze moulding technique, Ceram. Int. 42 (2016) 14843–14848, https://doi.org/10.1016/j.ceramint.2016.06.118.
[52] H. Hao, Y. Hao, X. Gao, M. Li, K. Qin, Wang, Effect of sintering temperature on property of low-density ceramic proppant adding coal gangue, Mater. Sci. 26 (2019) 94–98, https://doi.org/10.5755/j01.ms.26.1.19376.
[53] X. Chen, S. Li, Y. Shang, J. Wang, J. Zheng, In situ mullite whisker network formation for high strength and lightweight ceramic proppants, Process. Appl. Ceram. (2024), https://doi.org/10.2298/PAC2401077C.
[54] K.-B. Han, J. Graser, C.J. Robert, L. Martins de Mendonca Filho, J. McLennan, T. D. Sparks, Synthesis and microstructural evolution in iron oxide kaolinite based proppant as a function of reducing atmosphere, sintering conditions, and composition, Ceram. Int. 44 (2018) 9976–9983, https://doi.org/10.1016/j.ceramint.2018.03.047.
[55] R. Chen, Y. Li, R. Xiang, S. Li, Effect of particle size of fly ash on the properties of lightweight insulation materials, Constr. Build. Mater. 123 (2016) 120–126, https://doi.org/10.1016/j.conbuildmat.2016.06.140.
[56] X. Zou, The low temperature preparation of ultra low-density ceramic proppants by adding fly ash, Ceram. Silik. 64 (2019) 1–9, https://doi.org/10.13168/cs.2019.0055.
[57] X. Ma, Y. Tian, Y. Zhou, K. Wang, Y. Chai, Z. Li, Sintering temperature dependence of low-cost, low-density ceramic proppant with high breakage resistance, Mater. Lett. 180 (2016) 127–129, https://doi.org/10.1016/j.matlet.2016.04.080.
[58] P. Yang, F. Yan, S. Bi, Y. Zeng, L.B. Sim, Preliminary study on fully replacing bauxite with secondary aluminum ash in ceramsite proppants, Case Stud. Chem. Environ. Eng. 10 (2024) 101015, https://doi.org/10.1016/j.cscee.2024.101015.
[59] W. Jianguang, Z. Xiaofeng, F. Xiaofei, C. Yinghe, B. Fan, Experimental investigation of long-term fracture conductivity filled with quartz sand: mixing proppants and closing pressure, Int. J. Hydrog. Energy 46 (2021) 32394–32402, https://doi.org/10.1016/j.ijhydene.2021.07.083.
[60] W. Zheng, S.C. Silva, D.D. Tannant, Crushing characteristics of four different proppants and implications for fracture conductivity, J. Nat. Gas. Sci. Eng. 53 (2018) 125–138, https://doi.org/10.1016/j.jngse.2018.02.028.
[61] D. Guo, Y. Zhao, Z. Guo, X. Cui, B. Huang, Theoretical and experimental determination of proppant crushing rate and fracture conductivity, J. Energy Res. Technol. 142 (2020), https://doi.org/10.1115/1.4047079.
[62] Y. Liu, L. Wu, J. Guo, S. He, Y. Wu, Model for fracture conductivity considering particle size redistribution caused by proppant crushing, Geoenergy Sci. Eng. 240 (2024) 213081, https://doi.org/10.1016/j.geoen.2024.213081.
[63] G.D.C.C. Lucas, B.V. de Amorim, M.O. Rafael, Cruz, The choice of scaling technique matters for classification performance, Appl. Soft Comput. 133 (2023) 109924, https://doi.org/10.48550/arxiv.2212.12343.